

Scatter in the Relation between Persistent Radio Source Luminosity and Fast Radio Burst Rotation Measure: A Window into Circum-burst Environments

YUAN-PEI YANG ¹

¹*South-Western Institute for Astronomy Research, Yunnan Key Laboratory of Survey Science, Yunnan University, Kunming, Yunnan 650504, People's Republic of China; ypyang@ynu.edu.cn*

ABSTRACT

The association of persistent radio sources (PRSs) with repeating fast radio bursts (FRBs) offers unique insights into their circum-burst environments. Building upon the physical link between PRS luminosity (L_ν) and FRB rotation measure (RM), we introduce a novel diagnostic framework utilizing the intrinsic scatter of the $L_\nu - |\text{RM}|$ relation as a physical probe of nebula dynamics. We demonstrate that this scatter encodes critical information regarding the temporal evolution of the nebula radius ($R \propto t^\alpha$). By deriving a generic scaling $L_\nu \propto R^\epsilon |\text{RM}|$ and analyzing the residuals of the five confirmed FRB-PRS systems, we constrain the nebula's evolutionary index to $\alpha|\epsilon| = 1.5 \pm 0.7$ (1σ uncertainty). This measurement provides a powerful diagnostic tool for distinguishing among different astrophysical scenarios. Its value deviates from the expectations for supernova remnants (SNRs) in the Sedov-Taylor phase ($\alpha|\epsilon| \sim 0.2 - 0.4$), reverse shocks during the free-expansion phase of SNR/interstellar medium (ISM) interactions ($\alpha|\epsilon| \gtrsim 3.5$), and pulsar wind nebulae (PWNe) powered by a decaying wind ($\alpha|\epsilon| \sim 0 - 0.15$). Instead, it is more consistent with forward shocks in the free-expansion phase of both SNR/ISM and PWN/SNR systems ($\alpha|\epsilon| \sim 2.0 - 2.8$), and young PWNe driven by a nearly constant wind ($\alpha|\epsilon| \sim 1$). These findings suggest that active repeaters are powered by dynamically young, rapidly expanding nebulae. While currently limited by the small sample size, this framework establishes a robust methodology for future population studies to constrain the physical origin of PRSs.

Keywords: Compact radiation sources (289) — Radio transient sources (2008) — Radio bursts (1339) — Radio continuum emission (1340)

1. INTRODUCTION

Fast radio bursts (FRBs) are millisecond-duration radio transients at cosmological distances, characterized by extreme brightness temperatures that necessitate coherent radiation mechanisms. Up to the present, more than 4500 FRB sources have been detected and nearly 100 have been confirmed to be repeaters (CHIME/FRB Collaboration et al. 2021; FRB Collaboration et al. 2026). The association between FRB 200428 and the Galactic magnetar SGR J1935+2154 provides compelling evidence that at least a subset of FRBs can originate from magnetars (CHIME/FRB Collaboration et al. 2020; C. D. Bochenek et al. 2020; S. Mereghetti et al. 2020; C. K. Li et al. 2021; A. Ridnaia et al. 2021; M. Tavani et al. 2021). In contrast, the precise localization of FRB 20200120E to an exceptionally old globular cluster (M. Bhardwaj et al. 2021; F. Kirsten et al. 2022) challenges scenarios involving young magnetars formed

through core-collapse supernovae. Instead, this finding favors progenitor channels linked to older stellar populations, such as compact binary systems or alternative evolutionary pathways (J.-S. Wang et al. 2016; B. Zhang 2020; K. Kremer et al. 2021; W. Lu et al. 2022). These contrasting cases highlight the diversity of FRB progenitors and underscore the importance of identifying multi-wavelength counterparts for extragalactic FRBs (see the recent reviews of B. Zhang (2023, 2024)). To date, apart from host galaxies, persistent radio sources (PRSs) remain the only confirmed multiwavelength counterparts of extragalactic FRBs. These PRSs as compact sources near the FRB sources are physically distinct from the star-formation activity of their host galaxies and provide a unique window into the immediate circum-burst medium and the central engine of these FRB repeaters.

At present, five repeating FRBs have been securely associated with such compact PRSs (S. Chatterjee et al. 2017; C.-H. Niu et al. 2022; G. Bruni et al. 2024, 2025; Y. Bhusare et al. 2025; X. Zhang et al. 2025; A. L. Ibik et al. 2024; A. M. Moroianu et al. 2026). High-resolution

radio observations have revealed a remarkable diversity in their properties, spanning a wide range of specific luminosities (L_ν), spectral characteristics, and the Faraday rotation measures (RMs) of their associated bursts. Their key properties are summarized as follows:

- **FRB 20121102A:** As the prototype of this class residing in a dwarf galaxy at $z = 0.19273$ (S. P. Tendulkar et al. 2017), its associated PRS is physically compact (with a projected size < 0.7 pc, B. Marcote et al. (2017)) and highly luminous, with an observed peak specific luminosity of $L_{\nu,\text{peak}} \simeq 2.9 \times 10^{29} \text{ erg s}^{-1}\text{Hz}^{-1}$ at 1.6 GHz band (S. Chatterjee et al. 2017). The bursts exhibit an exceptionally high and decreasing RM of $|\text{RM}| \sim 10^4 - 10^5 \text{ rad m}^{-2}$ (D. Michilli et al. 2018; G. H. Hilmarsson et al. 2021) and a complex evolution of DM with a structural change (P. Wang et al. 2025), indicating an evolving extreme magneto-ionic environment. Significant flux variability was detected in this PRS covering the longest timescale recorded to date, with consistent amplitudes across short and long timescales (A. Y. Yang et al. 2024).
- **FRB 20190520B:** Often considered a “twin” to FRB 20121102A, this source is co-located with a compact PRS (with a projected size < 1.4 kpc) in a dwarf host galaxy at $z = 0.241$ (C.-H. Niu et al. 2022). The PRS luminosity is similarly high (with an observed peak specific luminosity of $L_{\nu,\text{peak}} \simeq 4.9 \times 10^{29} \text{ erg s}^{-1}\text{Hz}^{-1}$ at 1.5 GHz band). Notably, it exhibits a significantly decreasing host DM contribution ($\text{DM}_{\text{host}} \simeq 900 \text{ pc cm}^{-3}$) with a decay rate of $d\text{DM}/dt = -12.4 \text{ pc cm}^{-3}\text{yr}^{-1}$ (C.-H. Niu et al. 2026). Meanwhile, its highly variable RM showed dramatic sign reversals from $-36,000$ to $+20,000 \text{ rad m}^{-2}$ (R. Anna-Thomas et al. 2023), suggesting a turbulent, dense environment (Y.-P. Yang et al. 2023) or a binary system (F. Y. Wang et al. 2022; B. Zhang & R.-C. Hu 2025). The variability feature of the PRS light curve is similar to that associated with FRB 20121102A (A. Y. Yang et al. 2024).
- **FRB 20201124A:** Unlike the previous two, this source resides in a massive spiral galaxy at $z = 0.0979$ (W.-f. Fong et al. 2021). Deep VLA observations resolved a compact PRS (with a projected size < 0.7 kpc) distinct from the host’s diffuse star formation. It is significantly fainter (with an observed peak specific luminosity of $L_{\nu,\text{peak}} \simeq 7.9 \times 10^{27} \text{ erg s}^{-1}\text{Hz}^{-1}$ at 22 GHz) and exhibits an inverted spectrum of $F_\nu \propto \nu^{1.0}$ (G. Bruni et al.

2024), in contrast to the previous two. Its RM is comparatively lower, with values varying between -365 and -890 rad m^{-2} during the first 36 days of observations, followed by a stable, constant RM phase (H. Xu et al. 2022).

- **FRB 20240114A:** This active repeater exhibited unprecedented hyper-activity with over 11,000 bursts in 214 days, challenging standard magnetar models (J.-S. Zhang et al. 2025), and it is also associated with a PRS (with a projected size < 4 pc) in a sub-solar metallicity dwarf starburst galaxy at $z = 0.13056$ (G. Bruni et al. 2025; Y. Bhusare et al. 2025; X. Zhang et al. 2025). The PRS has an observed peak luminosity of $L_{\nu,\text{peak}} \simeq 3.5 \times 10^{28} \text{ erg s}^{-1}\text{Hz}^{-1}$ at 1.3 GHz (X. Zhang et al. 2025) and an RM of 338 rad m^{-2} (J. Tian et al. 2024).
- **FRB 20190417A:** Recently localized with milliarcsecond precision (with a projected size < 23 pc) at a star-forming galaxy at $z = 0.12817$, this source represents an extreme case with an exceeding DM contribution (A. M. Moroianu et al. 2026), like that of FRB 20190520B (C.-H. Niu et al. 2022). It is associated with a compact PRS (with an observed specific luminosity $L_{\nu,\text{peak}} \simeq 8.7 \times 10^{28} \text{ erg s}^{-1}\text{Hz}^{-1}$ at 1.4 GHz and possesses the largest known lower limit on the host DM contribution ($> 1228 \text{ pc cm}^{-3}$). Its RM is high and variable ($+4000$ to $+5000 \text{ rad m}^{-2}$), placing it in an intermediate regime between the prototypes and the fainter sources.

Despite their diverse host environments and spectral behaviors, these five systems collectively exhibit a broad, yet constrained, distribution in their specific luminosities (L_ν) and Faraday rotation measures (RMs). This growing sample suggests that PRSs may be a common feature of the repeating FRB population, rather than rare or exceptional associations. However, no PRS has been linked to a one-off FRB to date, implying a possible diversity in FRB progenitors or distinct emission mechanisms (T. An et al. 2025).

The nature of this nebula contributing PRS and RM remains a subject of open debate. Various possible scenarios have been proposed in the literature. Y.-P. Yang et al. (2016) first proposed that an FRB source embedded in a self-absorbed synchrotron nebula can heat nebular electrons through absorption process. The resulting hardened electron spectrum produces a spectral hump near the synchrotron self-absorption frequency, providing an observable signature of an embedded FRB. This model accounts for the observed special spectrum of the

PRS associated with FRB 20121102A (Q.-C. Li et al. 2020). The magnetar wind nebula scenario suggests that the PRS can originate from a young millisecond magnetar formed in a supernova or gamma-ray burst, powered by synchrotron emission from a magnetized wind nebula either through shocks interacting with the supernova ejecta (K. Murase et al. 2016; B. D. Metzger et al. 2017; B. Margalit & B. D. Metzger 2018; S. M. Rahaman et al. 2025) or directly with the surrounding interstellar medium (Z. G. Dai et al. 2017; Y.-H. Yang & Z.-G. Dai 2019). Alternatively, the “hypernebula” model proposed that a PRS can be produced by a nebula of relativistic electrons heated at the termination shock of super-Eddington disk winds and jets from a black hole or neutron star during a brief unstable mass-transfer phase in a binary system (N. Sridhar & B. D. Metzger 2022). Finally, accreting wandering massive black holes in dwarf galaxies represent another plausible origin for PRSs (T. Eftekhari et al. 2020; A. E. Reines et al. 2020; Y. Dong et al. 2024).

While the precise origin has yet to be determined, a physical connection between the burst source and the PRS can be generally inferred from the concurrent requirements for particle acceleration and Faraday rotation within a magnetized medium (Y.-P. Yang et al. 2020, 2022), also see Figure 1. First, the observed non-thermal continuum spectra of PRSs indicate the presence of relativistic electrons, which must be accelerated by energetic processes such as shocks or magnetized pair winds. Second, the large RMs imply that the radio bursts propagate through a dense, highly magnetized plasma. If the persistent synchrotron emission and the large Faraday rotation originate from the same physical volume—essentially a magnetized nebula surrounding the central engine—a generic correlation is expected between the specific luminosity of the PRS and the rotation measure ($L_\nu \propto |\text{RM}|$) as proposed by Y.-P. Yang et al. (2020, 2022). In this framework, a more luminous PRS, driven by higher energy injection or stronger magnetic fields, naturally corresponds to a denser magneto-ionic environment and, consequently, a larger $|\text{RM}|$. Such a “ $L_\nu - |\text{RM}|$ relation” has been confirmed by more and more detected PRSs (G. Bruni et al. 2024, 2025; A. L. Ibik et al. 2024; A. M. Moroiianu et al. 2026) and been applied to study the FRB cosmology (Z.-L. Zhang & B. Zhang 2025; R. Gao et al. 2025).

Generic nebular models predict a theoretical relation between PRS luminosity and FRB RM. However, observational data show a significant intrinsic scatter in the $L_\nu - |\text{RM}|$ plane. This scatter cannot be explained solely by measurement uncertainties, and it is likely physical, encoding vital information regarding the structural di-

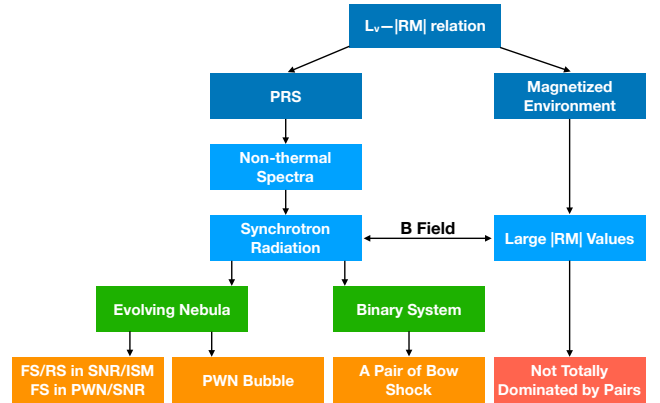


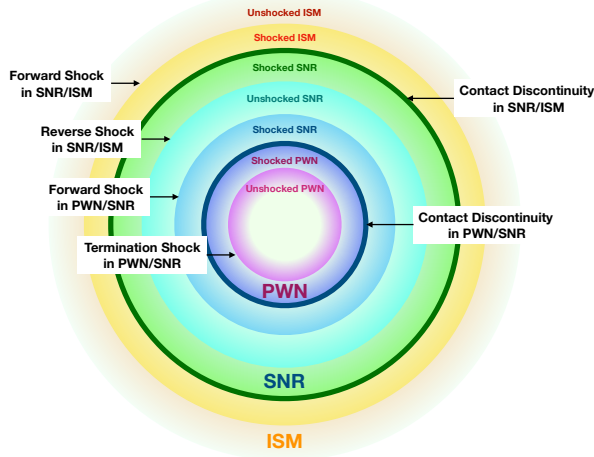
Figure 1. A flowchart showing the physical connections between PRS and RM. “FS”, “RS” and “TS” denotes forward shock, reverse shock and termination shock, respectively. Notice that the RS in a PWN/SNR system mainly generates X-ray emission and the radio emission is produced by fossil electrons in a PWN bubble.

versity of the circum-burst environments. In this work, we investigate the deviations of individual sources from the mean theoretical scaling. We demonstrate that this scatter provides a powerful diagnostic tool to constrain the physical radius distribution of the emitting nebulae and further infer the long-term evolution of the nebulae. The paper is organized as follows. In Section 2, we briefly summarize and further refine the theoretical framework of the $L_\nu - |\text{RM}|$ relation. In Section 3, we analyze how the scatter of the $L_\nu - |\text{RM}|$ relation reflect the distribution of the PRS-RM nebulae. In Section 4, we discuss the constraint on various candidate astrophysical scenarios that generate PRS-RM. Finally, the results are discussed and summarized in Section 5. Throughout this paper, the mathematical symbol “log” refers to the logarithm to base 10, and “ln” refers to the natural logarithm. The Λ CDM cosmological parameters in this work are taken as $\Omega_m = 0.315$ and $H_0 = 67.36 \text{ km s}^{-1} \text{ Mpc}^{-1}$ (Planck Collaboration et al. 2020).

2. THEORETICAL FRAMEWORK OF PRS LUMINOSITY – FRB RM RELATION

Y.-P. Yang et al. (2020, 2022) suggested that the large RM of an FRB repeater and its associated PRS may originate from the same physical region. Under this assumption, a generic relation can be established between the $|\text{RM}|$ value and the PRS specific luminosity, which depends only weakly on the specific PRS model. Considering that the relativistic electrons that emit non-thermal PRS should be from shocks or magnetized particle winds, the possible astrophysical scenarios can involve forward shock (FS) / reverse shock (RS) in a supernova remnant (SNR) / interstellar medium (ISM)

(a) various shocks in a PWN/SNR/ISM system



(b) a pair of bow shocks in a binary system

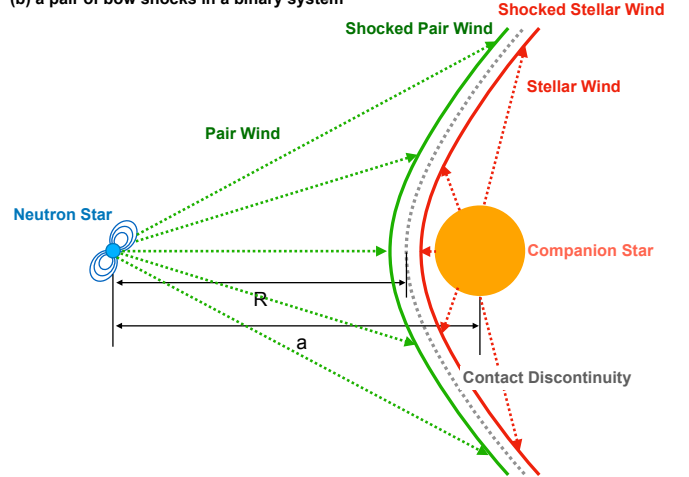


Figure 2. Various shocks in a PWN/SNR/ISM nebula (panel a) and a pair of bow shocks in a binary system (panel b).

system, FS / termination shock (TS) in a pulsar wind nebula (PWN) / SNR system, pulsar-wind/companion-wind bow shocks in a binary system. A flowchart is summarized in Figure 1 and the corresponding schematic diagram is shown in Figure 2. In all these scenarios, the bulk motion of the downstream and the contact discontinuity is usually non-relativistic in the observer frame², while the shock velocity relative to the unshocked medium can be either relativistic (e.g., TS in PWN, pair-wind bow shock in a binary system) or non-relativistic (e.g., the remaining scenarios mentioned above). The PRS-RM region can contain non-relativistic and/or relativistic electrons. We define the momentum distribution of all these electrons as $n_e(p) = n_{e,0}f(p)$, where $p = \sqrt{\gamma^2 - 1}$ is the dimensionless momentum and $p \simeq \gamma$ for $\gamma \gg 1$, γ is the Lorentz factor of electrons, $f(p) = n_e(p)/n_{e,0}$ with $\int f(p)dp = 1$ and $n_{e,0}$ is the total electron number density. In a relativistic context, the inertia of the electron increases, leading to the effective mass as $m_e^* \sim \gamma m_e$. Thus, in the PRS-RM region, the RM can be approximately written as ³

$$\text{RM} \simeq \frac{e^3}{2\pi m_e^2 c^4} \int_0^D ds \frac{n_{e,0} B_{\parallel}}{\gamma_c^2}, \quad (1)$$

² Relativistic bulk motion of the downstream primarily occurs in astrophysical contexts such as gamma-ray bursts and active galactic nuclei; however, in both cases, it is highly unlikely to be related to the origin of FRBs.

³ In a more rigorous treatment, accounting for the anisotropy of electron momentum in a magnetic field and assuming an ultra-relativistic Maxwellian distribution, a logarithmic term in the Lorentz factor, $\ln \gamma/2$, appears in the integrand (E. Quataert & A. Gruzinov 2000). Given that $\ln \gamma/2$ is of order unity and the specific form of the ultra-relativistic Maxwellian distribution, this logarithmic term is neglected in this work. This approximation has a negligible impact on the final results.

and the critical electron Lorentz factor is defined by

$$\gamma_c \equiv \left(\int_0^{\infty} dp \frac{f(p)}{1+p^2} \right)^{-1/2}. \quad (2)$$

where $\gamma = \sqrt{1+p^2}$ is used in the above formula. For the non-relativistic regime, the RM is given by the classical formula due to $\gamma_c \sim 1$; while for the relativistic regime, the RM is suppressed by a factor of $\sim \gamma_c^2$. As shown in Eq.(1), the properties of the electron momentum distribution play a key role in determining the magnitude of the RM. In particular, the large |RM|s observed in some repeating FRBs suggest that low-energy electrons dominate in the region responsible for the RM.

In the distribution of $f(p)$, electrons above a certain momentum of p_{obs} will produce the observed GHz wave via synchrotron radiation. We consider the synchrotron radiation from relativistic electrons under the magnetic field B in the PRS-RM region. The radiation power for a single electron is $P = (4/3)\sigma_T c \gamma^2 B^2 / 8\pi$, and the characteristic frequency is $\nu = \gamma^2 e B / 2\pi m_e c$. Thus, the specific power is $P_{\nu} \simeq P/\nu = m_e c^2 \sigma_T B / 3e$ and it is independent of ν . For a given observed frequency $\nu \sim 1$ GHz, the corresponding electrons are required to have a momentum of

$$\begin{aligned} p_{\text{obs}} \simeq \gamma_{\text{obs}} &\sim \left(\frac{2\pi m_e c \nu}{e B} \right)^{1/2} \\ &\simeq 600 \left(\frac{\nu}{1 \text{ GHz}} \right)^{1/2} \left(\frac{B}{1 \text{ mG}} \right)^{-1/2}. \end{aligned} \quad (3)$$

Since the bulk motion of the PRS-RM region should be non-relativistic for the possible scenarios we are interested here, e.g., PWN, SNR and binary system, the emission frequency at the bulk motion frame is approximately equal to that in the observer frame. We further

define ζ_e as the fraction of electrons that radiate synchrotron emission in the GHz band, then the fraction ζ_e is given by $\zeta_e \equiv F(> p_{\text{obs}})$,

$$\zeta_e \equiv F(> p_{\text{obs}}) = \int_{p_{\text{obs}}}^{\infty} dp f(p), \quad (4)$$

where $F(> p)$ is the cumulative distribution function (CDF) associated with the probability density function (PDF) $f(p)$. We consider that the PRS-RM region has a radius of R and a thickness of ΔR , then total number of relativistic electrons that emits GHz wave is approximately $N_e \simeq 4\pi R^2 \Delta R \zeta_e n_e / 3$ for $\Delta R \sim R$. The specific luminosity of synchrotron radiation is given by $L_\nu = N_e P_\nu$ (Y.-P. Yang et al. 2020, 2022)

$$L_\nu = \frac{64\pi^3}{27} \zeta_e \gamma_c^2 m_e c^2 R^2 |\text{RM}| \simeq 5.7 \times 10^{29} \text{ erg s}^{-1} \text{ Hz}^{-1} \times \left(\frac{\zeta_e \gamma_c^2}{0.01} \right) \left(\frac{R}{1 \text{ pc}} \right)^2 \left(\frac{|\text{RM}|}{10^3 \text{ rad m}^{-2}} \right). \quad (5)$$

where the factor of $\zeta_e \gamma_c^2$ only depends the electron momentum distribution and the observed frequency, and it can be calculated by

$$\zeta_e \gamma_c^2 = \left(\int_0^{\infty} dp \frac{f(p)}{1+p^2} \right)^{-1} \int_{p_{\text{obs}}}^{\infty} dp f(p). \quad (6)$$

The above PRS luminosity–FRB RM relation $L_\nu \propto \zeta_e \gamma_c^2 R^2 |\text{RM}|$ in Eq.(5) has the following implications and considerations:

- In the $L_\nu - |\text{RM}|$ relation, since the RM is contributed only by the line-of-sight component of the magnetic field, whereas the PRS depends on the total magnetic field strength, we emphasize that, in practice, it is suggested to be taken to be the maximum observed value of $|\text{RM}|$ as an estimator.
- Due to the large RM uncertainty of the host interstellar medium, the data with $|\text{RM}| \lesssim 10^2 - 10^3 \text{ rad m}^{-2}$ might substantially deviate from the predicted relation. However, for a sufficiently large sample in the future, one can mainly focus on the sample with $|\text{RM}| \gtrsim 10^2 - 10^3 \text{ rad m}^{-2}$ (as appeared in the current PRS sample). In this case, the host RM contribution can be neglected.
- $|\text{RM}|$ can be a function of the nebula radius R in the proposed nebula models (e.g., Y.-P. Yang et al. 2016; K. Murase et al. 2016; B. D. Metzger et al. 2017; B. Margalit & B. D. Metzger 2018), but it also depends on other physical quantities, such as the magnetic field, gas density, the initial mass and kinetic energy of the SN ejecta, etc. In

this case, the correlation between L_ν and $|\text{RM}|$ can even deviate from a power-law index of 1 more or less. However, as we will prove as below, one can still fit the observed data with $L_\nu \propto |\text{RM}|$ and the corresponding scatter will reflect the distribution of the nebula radius R in this case.

3. IMPLICATION OF SCATTER IN $L_\nu - |\text{RM}|$ RELATION

We have demonstrated that, for a given observed frequency (e.g., $\nu \sim 1, \text{GHz}$), the factor $\zeta_e \gamma_c^2$ is primarily determined by the electron distribution function $f(p)$. In an evolving nebula, e.g., SNR or PWN, the electron distribution $f(p)$ changes as the nebula expands. As a result, $\zeta_e \gamma_c^2$ becomes largely dependent on the nebular radius R (see Section 4 for details). This implies that, for an evolving nebula, $\zeta_e \gamma_c^2$ can be treated as a function of the nebular radius R . Accordingly, the above $L_\nu - |\text{RM}|$ relation can be written in a more general form as

$$L_\nu \propto R^\epsilon |\text{RM}|. \quad (7)$$

where ϵ is a power-law index. *In this case, the distribution of the nebula radius leads to the scatter of the $L_\nu - |\text{RM}|$ relation.*

3.1. Methodology

First, we derive how the observed scatter in the $L_\nu - |\text{RM}|$ relation constrains the evolution of nebular radius. In most scenarios of interest, the distribution of nebular radii is primarily determined by their ages⁴. We first generally consider the time evolution of the nebula radius as

$$R \propto t^\alpha, \quad (8)$$

where α is the temporal index of the nebula radius evolution. Such a power-law evolution is consistent with the scenarios of PWN and SNR (S. P. Reynolds & R. A. Chevalier 1984; C. F. McKee & J. K. Truelove 1995; E. van der Swaluw et al. 2001), also see Table 1 in a summary. We assume that the formation rate of the PRS sources is steady, in which case, the source number is proportional to the source age. Thus, the CDF of the nebula radius is given by

$$F(< R) \propto R^{1/\alpha}. \quad (9)$$

⁴ Note that in the bow shock scenario within a binary system, the bow-shock nebula radius does not evolve with time and is instead primarily determined by the orbital separation (see Section 4.3). This contrasts with expanding nebulae, whose sizes increase progressively as they age.

Table 1. Radius Evolution of various shocks and bubbles in a PWN/SNR/ISM system

		FS in SNR/ISM	RS in SNR/ISM	FS in PWN/SNR	PWN Bubble
Free Expansion		$R \propto t, V_{\text{sh}} \sim \text{const.}$	$R \sim t, V_{\text{sh}} \propto t^{3/2}$	$R \propto t^{6/5}, V_{\text{sh}} \propto t^{1/5}$	$R \propto t^{6/5}$
Sedov-Taylor	Constant Wind	$R \propto t^{2/5}, V_{\text{sh}} \propto t^{-3/5}$	Shock absent	Shock absent	$R \propto t^{11/15}$
	Decaying Wind	$R \propto t^{2/5}, V_{\text{sh}} \propto t^{-3/5}$	Shock absent	Shock absent	$R \propto t^{3/10}$

Notes: “FS”, “RS” and “TS” denotes forward shock, reverse shock and termination shock, respectively. R is the shock/bubble radius and V_{sh} is the shock velocity related to the upstream. During the Sedov–Taylor phase, the RS in the SNR/ISM system has completely swept through all of the SN ejecta, and the shock radius approaches the center of the SNR. Since this RS reheats the SNR ejecta, the sound velocity increases by a large factor, which causes that the FS in the PWN/SNR system has also been absent (E. van der Swaluw et al. 2001). For the RS in the SNR/ISM system, the shock velocity related to the upstream is $V_{\text{sh}} = R/t - dR/dt$. Due to the contribution of an additional second-order small quantity $t^{5/2}$ (C. F. McKee & J. K. Truelove 1995), a time-dependent shock velocity is obtained. In particular, for the PWN bubble scenario, the radio radiation is emitted by fossil electrons in the bubble. In this case, R denotes the bubble radius (i.e., the contact discontinuity) and the shock velocity is omitted here.

Using the definition of $x \equiv \ln R$, the above CDF can be written as $F(< x) \propto e^{x/\alpha}$. Assuming the range of R is sufficiently large, $\ln(R_{\text{max}}/R_{\text{min}}) \gg \alpha$, where R_{max} and R_{min} are the maximum and minimum nebula radius, respectively, the truncated exponential distribution can be approximated by a semi-infinite distribution. Under this assumption, the standard deviation of x is given by $\sigma_x = \alpha$, leading to $\sigma_{\ln R} \simeq \alpha$. Converting this back to the base-10 logarithm using the change of base formula $\log R = \ln R / \ln 10$, one finally has

$$\sigma_{\log R} \simeq \frac{\alpha}{\ln 10}. \quad (10)$$

Therefore, once $\sigma_{\log R}$ is measured, we will know how the nebula radius evolve as time.

Next, we propose that $\sigma_{\log R}$ can be measured by the scatter of the $L_\nu - |\text{RM}|$ relation. We consider the measured data as $(\log L_{\nu,i}, \log |\text{RM}|_i)$ with $i = 1, 2, 3, \dots, N$, where N is the number of the data. The data satisfy the potential physical relation of $L_{\nu,i} = kR_i^\epsilon |\text{RM}|_i$, which can be equivalently expressed as

$$\log L_{\nu,i} = \log |\text{RM}|_i + \epsilon \log R_i + \log k, \quad (11)$$

where R_i is the nebula radius as a random variable for each source, and k is a constant. We first fit the observational data $(\log L_{\nu,i}, \log |\text{RM}|_i)$ using the following fitting function of

$$\log L_{\nu,\text{fit}} = \log |\text{RM}| + C_0, \quad (12)$$

where C_0 is the intercept determined by the ordinary least squares method, ensuring the mean residual is zero,

$$C_0 = \langle \log L_{\nu,i} - \log |\text{RM}|_i \rangle = \epsilon \langle \log R_i \rangle + \log k. \quad (13)$$

Notice that, regardless of whether RM is physically related to R (for example, $|\text{RM}| \propto R^\delta$), we deliberately enforce a positive correlation with a unit slope to fit the

observational data, namely $L_\nu \propto |\text{RM}|$. The detailed reasons for this choice will be explained in detail in the following Section 3.3. We then define the residual Δ for each data point as the difference between the observed value and the fitted value. Subtracting Eq.(12) from Eq.(11), $\Delta_i = \log L_{\nu,i} - \log L_{\nu,\text{fit},i}$, the residuals simplify to

$$\Delta_i = \epsilon(\log R_i - \langle \log R_i \rangle). \quad (14)$$

Since the residuals must be centered at zero for any reasonable fitting algorithm, i.e., $\langle \Delta_i \rangle = 0$, the observed dispersion (standard deviation) of the residuals, σ_Δ , is directly related to the standard deviation of $\log R$,

$$\sigma_\Delta = |\epsilon| \sigma_{\log R}. \quad (15)$$

Substituting Eq.(10) and Eq.(15), we obtain the analytical expression connecting the observed scatter to α

$$\alpha = \ln 10 \left(\frac{\sigma_\Delta}{|\epsilon|} \right). \quad (16)$$

This result shows that the observed scatter directly measures the evolutionary index of the nebula. Since $\log R$ has been considered to satisfy approximately an exponential distribution, The uncertainty of α is estimated based on the asymptotic variance of the maximum likelihood estimator for an exponential scale parameter, given by $\sigma_\alpha \simeq \alpha/\sqrt{N}$, leading to

$$\sigma_\alpha \simeq \frac{\ln 10}{\sqrt{N}} \left(\frac{\sigma_\Delta}{|\epsilon|} \right), \quad (17)$$

for $|\delta\epsilon/\epsilon| \lesssim |\delta\alpha/\alpha|$. Based on the above result, in order to distinguish between various models with a difference of $\Delta\alpha$ larger than $3\sigma_\alpha$, the data number should satisfy

$$N > 9 \left(\frac{\alpha}{\Delta\alpha} \right)^2 \sim \mathcal{O}(10). \quad (18)$$

Therefore, we expect that a sample with $N \gg 10$ will be helpful to diagnose the physical origin of PRSs within 3σ .

Table 2. FRB-PRS sample considered in this work

FRB Name	z^a	d_L^b (Gpc)	RM ^c (rad m ⁻²)	F_ν^d (μ Jy)	ν^e (GHz)	L_ν^f (10^{29} erg s ⁻¹ Hz ⁻¹)	References ^g
FRB 20121102A	0.19273	0.98	1.46×10^5	203	6	2.3	1,2,3,4
FRB 20190520B	0.241	1.25	-3.6×10^4	152	5.5	2.8	5,6
FRB 20201124A	0.0979	0.47	-889.5	8.2	6	0.022	7,8,9
FRB 20240114A	0.13056	0.64	338.1	46	5	0.22	10,11,12,13,14
FRB 20190417A	0.12817	0.62	5061	190	1.4	0.87	15

Notes:

^aThe measured redshifts of the host galaxies of FRBs.

^bThe luminosity distance calculated by redshift. The Λ CDM cosmological parameters are taken as $\Omega_m = 0.315$, $\Omega_b h^2 = 0.02237$, and $H_0 = 67.36$ km s⁻¹ Mpc⁻¹ (Planck Collaboration et al. 2020).

^cThe observed RMs of FRBs. Here, we take the largest absolute value for the observed RMs.

^dThe observed PRS flux densities are primarily taken from measurements at 5–6 GHz, where data are available for most PRSs. For FRB 20190417A, which lacks observations in this band, we instead use its 1.4 GHz flux density.

^eTo ensure consistency with the theoretical framework developed in this work, we adopt a uniform observed frequency of 5–6 GHz for all sources, except for FRB 20190417A.

^fThe specific luminosities of the PRS inferred by the observed flux density and distance.

^gReferences: (1) S. Chatterjee et al. (2017), (2) S. P. Tendulkar et al. (2017), (3) D. Michilli et al. (2018), (4) G. H. Hilmarsson et al. (2021), (5) C.-H. Niu et al. (2022), (6) R. Anna-Thomas et al. (2023), (7) W.-f. Fong et al. (2021), (8) H. Xu et al. (2022), (9) G. Bruni et al. (2024), (10) J.-S. Zhang et al. (2025), (11) G. Bruni et al. (2025), (12) X. Zhang et al. (2025), (13) Y. Bhusare et al. (2025), (14) J. Tian et al. (2024), (15) A. M. Moroianu et al. (2026).

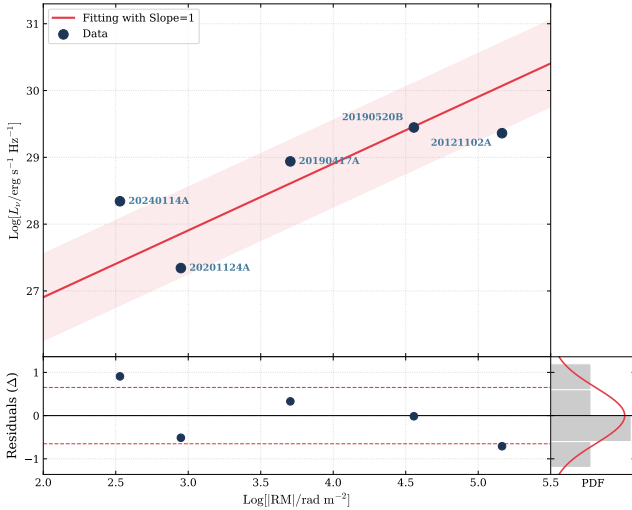


Figure 3. The $L_\nu - |\text{RM}|$ relation with the current five sources. Top panel: The observed data points are shown as black circles, labeled with their respective event IDs. The solid red line represents the best-fit linear model with a fixed slope of unity. The red shaded region indicates the scatter (standard deviation) of the data around the best-fit line, with $1\sigma = 0.65$. Bottom panels: The left panel displays the residuals (Δ) of the fit in logarithmic scale. The horizontal red dashed lines mark the $\pm 1\sigma$ boundaries. The right panel shows the distribution of these residuals, overlaid with a Gaussian profile (solid red curve) derived from the sample statistics.

3.2. Data Analysis of Observational Sample

In this section, we measure $\alpha|\epsilon|$ based on the current five PRSs, with detail information shown in Table 2. Given that most PRSs have observational data

available in the 5–6 GHz band, while FRB 20190417A has so far only been observed at 1.4 GHz, we primarily adopt the flux densities measured at 5–6 GHz. For FRB 20190417A, due to the lack of observations in this frequency range, we temporarily use its flux density measured at 1.4 GHz. Notice that since the observational uncertainties in both PRS flux densities and FRB RMs are significantly smaller than the derived intrinsic scatter, the impact of measurement errors is negligible and thus omitted in our statistical framework. The data processing algorithm first applies a base-10 logarithmic transformation to the variables L_ν and $|\text{RM}|$. A linear model defined as $\log L_{\nu,\text{fit}} = \log |\text{RM}| + C_0$ is fitted to the data ($\log L_{\nu,i}, \log |\text{RM}|_i$) by calculating C_0 as the mean difference between the observed logarithmic values, $C_0 = \langle \log L_\nu - \log |\text{RM}| \rangle$. Subsequently, the residuals are computed using the equation $\Delta = \log L_\nu - \log L_{\nu,\text{fit}}$. Finally, the dispersion of the data is quantified by determining the standard deviation of these residuals, σ_Δ . Based on the above method, we obtain

$$\sigma_\Delta = 0.65, \quad (19)$$

The fitting result and the standard deviation are shown in Figure 3. According to Eq.(16) and Eq.(17), this yields

$$\alpha|\epsilon| = 1.5 \pm 0.7. \quad (20)$$

with 1σ error. We caution that Eq.(17) is derived based on the asymptotic variance of the maximum likelihood estimator, which formally applies to large samples. For

our current small sample size ($N = 5$), the derived 1σ uncertainty (± 0.7) should be treated as a lower limit of the true statistical error. Future validation using a larger sample or bootstrapping methods is required. In the following Section 4, we will constrain the astrophysical scenarios based on the above measured value.

3.3. Mathematical Robustness

A critical concern in our analysis is the potential unknown correlation between the independent variable RM and the stochastic variable R . Physically, these quantities might be coupled through an underlying function $|\text{RM}| = g(R, X)$, where X denotes other physical parameters like electron number density n_e and magnetic field strength B in ISM, which would imply that the intrinsic relationship between $\log L_\nu$ and $\log |\text{RM}|$ may deviate from a linear function with a slope of unity. This raises the question of whether fitting a fixed-slope model ($\log L_\nu = \log |\text{RM}| + C_0$) is mathematically justifiable and whether the derived α is biased by this assumption.

Mathematically, the validity of our method does not rely on $|\text{RM}|$ and R being independent. The governing physical equation is defined as $L_\nu = kR^\epsilon |\text{RM}|$. By fixing the slope to unity during the residual calculation, we perform a ‘‘physical detrending’’ rather than a statistical best-fit. The residual Δ is defined as $\Delta = \log L_\nu - \log |\text{RM}| - C_0 = \epsilon \langle \log R_i \rangle + \log k$. This algebraic subtraction strictly isolates the contribution of R , regardless of whether $|\text{RM}|$ itself is a function of R . Consequently, the observed residual Δ remains a direct proxy for $\log R$. If a correlation exists (e.g., $|\text{RM}| \propto R^\delta$), it manifests as a systematic trend (tilt) in the residuals versus $\log |\text{RM}|$. However, the global dispersion σ_Δ calculated over the entire sample correctly integrates both the intrinsic stochasticity of R and the variation of R induced by its coupling with RM. Thus, σ_Δ faithfully reflects the total dynamic range of R within the observed sample.

4. CONSTRAINTS ON VARIOUS ASTROPHYSICAL SCENARIOS

Accumulating observational evidence suggests that the central engine of fast radio bursts (FRBs) is a neutron star, as exemplified by the Galactic event associated with SGR J1935+2154 (CHIME/FRB Collaboration et al. 2020; C. D. Bochenek et al. 2020; S. Mereghetti et al. 2020; C. K. Li et al. 2021; A. Ridnaia et al. 2021; M. Tavani et al. 2021). Motivated by this picture, several astrophysical scenarios can be considered for the origin of the magnetized environment responsible for both the observed RM and the associated PRS.

Broadly, these scenarios can be classified into the following categories: (1) *Non-relativistic shock systems in*

nebulae, including FS and RS in the SNR/ISM system, as well as FS formed in the PWN/SNR system, see the panel (a) of Figure 2; (2) *PWN bubble*, where relativistic fossil electron pairs are filling the region between the TS and the contact discontinuity in the PWN/SNR system, see the panel (a) of Figure 2; (3) *Binary bow-shock systems*, in which a bow shock is formed through the interaction between the pulsar wind and the wind of a companion star, see the panel (b) of Figure 2.

4.1. non-relativistic shock in nebula

We first discuss the case of non-relativistic shocks in SNR and PWN, including FS/RS in the SNR/ISM system and FS in the PWN/SNR system, as shown in the panel (a) of Figure 2. The observed non-thermal radiation of PRSs implies that they are most likely to originate from relativistic electrons accelerated by shock. The thermal kinetic energy of electrons in the downstream of a non-relativistic shock wave is

$$E_{\text{th}} \equiv k_B T = \frac{1}{2} \epsilon_e m_p V_{\text{sh}}^2, \quad (21)$$

where ϵ_e is the proportion of thermal energy obtained by downstream electrons to the total available kinetic energy, V_{sh} is the shock velocity related to the upstream, respectively. We define the corresponding thermal momentum of electrons as p_{th} . In non-relativistic regime, $p_{\text{th}} \simeq \sqrt{2m_e E_{\text{th}}}$, leading to

$$p_{\text{th}} \sim \epsilon_e (m_e m_p)^{1/2} V_{\text{sh}}. \quad (22)$$

The next question is how many electrons are accelerated by the shock. The electron injection problem in collisionless shocks arises from the scale disparity between the electron Larmor radius and the shock transition width, necessitating a pre-acceleration mechanism to elevate electrons from the thermal pool to a threshold momentum, p_{inj} , required for diffusive shock acceleration (DSA). This threshold typically scales as a small multiple of the thermal momentum,

$$p_{\text{inj}} = \xi p_{\text{th}}, \quad (23)$$

because it represents the optimal intersection between the super-thermal tail of the Maxwellian distribution and the kinematic requirement to outrun downstream advection. Below p_{inj} , the electrons satisfy a thermalized Maxwellian distribution; and above p_{inj} , the electrons satisfy a power-law distribution. The independence of the ratio of $\xi \equiv p_{\text{inj}}/p_{\text{th}}$ from extrinsic parameters stems from the self-similar nature of shock microphysics: since both the downstream thermalization and the generation of mediating electromagnetic turbulence are self-consistently driven by the same reservoir of upstream

ram pressure for strong shocks, the characteristic scales of the system scale proportionally, preserving the injection threshold as a universal constant of the normalized distribution.

For non-relativistic shock, most electrons in the downstream satisfy the Maxwell-Boltzmann distribution,

$$f(p)dp = \frac{4}{\sqrt{\pi}p_{\text{th}}} \left(\frac{p}{p_{\text{th}}}\right)^2 \exp\left[-\left(\frac{p}{p_{\text{th}}}\right)^2\right] dp, \quad (24)$$

with $p_{\text{th}} = \sqrt{2m_e k_B T} \propto V_{\text{sh}}$ given by Eq.(22). The peak momentum is $p_{\text{peak}} \simeq p_{\text{th}}$. We consider that a part of electrons are accelerated above ξp_{th} and the accelerated electrons satisfy a power-law distribution of

$$f(p)dp \propto \left(\frac{p}{p_{\text{inj}}}\right)^{-s} dp \quad \text{with } p_{\text{inj}} = \xi p_{\text{th}}. \quad (25)$$

Combining the above two distribution, one has

$$f(p)dp = f(z)dz \propto \begin{cases} z^2 e^{-z^2} dz, & z \ll \xi \\ \xi^2 e^{-\xi^2} \left(\frac{z}{\xi}\right)^{-s} dz. & z \gg \xi \end{cases} \quad (26)$$

with $z \equiv p/p_{\text{th}}$. The CDF is

$$\begin{aligned} \zeta_e \equiv F(> p_{\text{obs}}) &= \left(\frac{x_{\text{obs}}}{\xi}\right)^{1-s} \\ &\times \frac{4\xi^3}{\sqrt{\pi}(s-1)e^{\xi^2} \text{erf}(\xi) + 2\xi(2\xi^2 - s + 1)} \propto \left(\frac{p_{\text{obs}}}{p_{\text{th}}}\right)^{1-s} \\ &\propto V_{\text{sh}}^{s-1}, \end{aligned} \quad (27)$$

where $\text{erf}(\dots)$ is the Gauss error function. We assume that the relation between the shock radius and the shock velocity as

$$V_{\text{sh}} \propto R^{\beta_V}. \quad (28)$$

According to the predicted $L_\nu - |\text{RM}|$ relation and $\gamma_c \sim 1$ in non-relativistic regime, one finally has

$$L \propto \zeta_e \gamma_c^2 R^2 |\text{RM}| \propto R^\epsilon |\text{RM}| \quad \text{with } \epsilon = 2 + \beta_V(s-1). \quad (29)$$

Since we have considered the shock radius evolve as $R \propto t^\alpha$, for the FSs in both the SNR/ISM system and the PWN/SNR system, the shock velocity evolves with $V_{\text{sh}} \propto t^{\alpha-1} \propto R^{(\alpha-1)/\alpha}$, leading to $\beta_V = (\alpha-1)/\alpha$. Therefore, 1) in the free-expansion phase, the FS in the SNR/ISM system has $\alpha = 1$ and $\beta_V = 0$, leading to $\epsilon = 2$ and $\alpha|\epsilon| = 2$; the FS in the PWN/SNR system has $\alpha = 6/5$ and $\beta_V = 1/6$, leading to $\epsilon = 2.2, 2.3$ and $\alpha|\epsilon| = 2.6, 2.8$ for $s = 2, 3$, respectively. 2) in the

Table 3. The theoretical values of the combined index $\alpha|\epsilon|$ for various shock scenarios compared with the measured value of $\alpha|\epsilon| = 1.5 \pm 0.7$

		$\alpha \epsilon $	
		$s = 2.0$	$s = 3.0$
FS in SNR/ISM	Free-Expansion	2.0	2.0
FS in PWN/SNR	Free-Expansion	2.6	2.8
FS in SNR/ISM	Sedov-Taylor	0.2	0.4
RS in SNR/ISM	Free-Expansion	3.5	5.0

Sedov-Taylor phase, the FS in the SNR/ISM system has $\alpha = 2/5$ and $\beta_V = -3/2$, leading to $\epsilon = 0.5, -1$ and $\alpha|\epsilon| = 0.2, 0.4$ for $s = 2, 3$, respectively; the FS in the PWN/SNR system has been absent in this stage.

For the RS in the SNR/ISM system, in the free-expansion phase, $R \propto t$ and $V_{\text{sh}} \propto t^{3/2}$ (We should note that due to the contribution of an additional second-order small quantity $t^{5/2}$ (C. F. McKee & J. K. Truelove 1995), a time-dependent shock velocity is obtained), one has $\alpha = 1$ and $\beta_V = 3/2$, leading to $\epsilon = 3.5, 5.0$ and $\alpha|\epsilon| = 3.5, 5.0$ for $s = 2, 3$, respectively; in the Sedov-Taylor phase, the RS in the SNR/ISM system has been absent. All the results are summarized in Table 3. In conclusion, the measured value of $\alpha|\epsilon| = 1.5 \pm 0.7$ disfavors SNRs in the Sedov-Taylor phase and reverse shocks during the free-expansion phase of SNR/ISM interactions, while being more consistent with forward shocks in the free-expansion phase of both SNR/ISM and PWN/SNR systems.

4.2. PWN Bubble

In the above scenarios, the relativistic electrons with $\gamma \sim (10^2 - 10^3)$ that produces radio emission are accelerated by the shocks in SNR and ISM. However, in the TS of PWN, two different components of the relativistic electrons are to be distinguished (e.g., A. M. Atoyan & F. A. Aharonian 1996; B. M. Gaensler & P. O. Slane 2006; L. Zhang et al. 2008), namely (a) the population of freshly accelerated ultrarelativistic electrons which are being presently injected downstream of the wind shock (so-called the wind electrons), and (b) the population of electrons of lower energies responsible for the radio emission, which are, presumably, ‘relic’ and reflect the PWN history (so-called the fossil electrons). The wind electrons and the fossil electrons have a Lorentz factor of $\gamma \sim (10^4 - 10^6)$ and $\gamma \sim (10^2 - 10^3)$, respectively, which mainly produce the X-ray and radio emissions, respectively. The typical radio luminosity of PWNe ranges from $10^{28} \text{ erg s}^{-1}$ to $10^{36} \text{ erg s}^{-1}$ (D. A. Frail & B. R. Scharringhausen 1997). In this work, since the PRSs are

emitted at the radio band, we mainly focus on the fossil electrons. For the fossil electrons that emit the radio radiation, according to Eq.(3), the synchrotron cooling timescale is estimated by

$$\begin{aligned} \tau_{\text{syn}} &= \frac{6\pi m_e c}{\sigma_T B^2 \gamma} \\ &\simeq 4.1 \times 10^4 \text{ yr} \left(\frac{B}{1 \text{ mG}} \right)^{-3/2} \left(\frac{\nu}{1 \text{ GHz}} \right)^{-1/2}, \end{aligned} \quad (30)$$

which is most likely longer than the age of the nebula, meanwhile, the synchrotron cooling process can be ignored. Due to the low energies and long radiative lifetime of fossil electrons, these particles are expected to be dominated by those previously injected into the PWN by the central neutron star, and therefore their spectrum reflects the evolution of the PWN during its history. In this case, the fossil electrons are homogeneously distributed in the nebula with a radius at the contact discontinuity in the PWN/SNR system (shown in the panel (a) of Figure 2), and we term it the PWN bubble in this work, which also agrees with the diffuse radio maps of the Crab Nebula. In observation, the fossil electrons are proposed to have a distribution of $n_e(\gamma)d\gamma \propto \gamma^{-s}$ with $s \sim (1 - 1.5)$ for $\gamma > \gamma_m$ (e.g., A. M. Atoyan & F. A. Aharonian 1996; B. M. Gaensler & P. O. Slane 2006; L. Zhang et al. 2008).

The nebula bubble radius R is determined by the evolutionary stage of the PWN/SNR system and the spindown of the neutron star (e.g., E. van der Swaluw et al. 2001, also see Table 1). In the free-expansion phase, the PWN bubble radius evolve as $R \propto t^{6/5}$. In the Sedov-Taylor phase, the bubble radius evolution determines whether the neutron star is in the spindown phase: 1) if the system age is smaller than the spindown timescale, the spindown luminosity is a constant, leading to a constant wind. In this case, the PWN bubble radius evolve as $R \propto t^{11/15}$; 2) if the system age is longer than the spindown timescale, the spindown luminosity decreases t^{-2} , leading to a decaying wind. In this case, the PWN bubble radius evolve as $R \propto t^{3/10}$.

In order to obtain how the factor $\zeta_e \gamma_c^2$ evolves with the bubble radius R , we need first analyze the distribution evolution of the fossil electron. For the fossil electrons in a PWN bubble, the synchrotron cooling can be ignored and the dominated cooling process is adiabatic process. Thus, the kinetic equation of electron distribution can be written as

$$\frac{\partial N_e(\gamma, t)}{\partial t} + \frac{\partial}{\partial \gamma} [\dot{\gamma}_{\text{ad}} N_e(\gamma, t)] = Q(\gamma, t). \quad (31)$$

Assuming that the PWN expands adiabatically, one has the pressure $P \propto V^{-4/3} \propto R^{-4}$ for relativistic gas. The

total internal energy is $U = N_e \gamma m_e c^2 = 3PV \propto R^{-1}$, finally leading to $\gamma \propto R^{-1}$ and $\dot{\gamma}_{\text{ad}} = -(\dot{R}/R)\gamma$. Assuming $R \propto t^\alpha$ and defining $Q = (s-1)(\dot{N}_e/\gamma_m)(\gamma/\gamma_m)^{-s}$ for $\gamma > \gamma_m$ and $Q = 0$ for $\gamma < \gamma_m$, the kinetic equation can be rewritten as

$$\frac{\partial N_e(\gamma, t)}{\partial t} - \frac{\alpha}{t} \frac{\partial}{\partial \gamma} [\gamma N_e(\gamma, t)] = (s-1) \frac{\dot{N}_e}{\gamma_m} \left(\frac{\gamma}{\gamma_m} \right)^{-s} \quad (32)$$

It can be solved as

$$\begin{aligned} N_e(\gamma, t) &= \frac{(s-1) \dot{N}_e t}{1 + \alpha(s-1) \gamma_m} \\ &\times \begin{cases} \left(\frac{\gamma}{\gamma_m} \right)^{1/\alpha-1}, & \gamma_m(t/t_0)^{-\alpha} < \gamma < \gamma_m, \\ \left(\frac{\gamma}{\gamma_m} \right)^{-s}, & \gamma > \gamma_m. \end{cases} \end{aligned} \quad (33)$$

The electron number density is $n_e(\gamma, t) = N_e(\gamma, t)/V(t) \propto t^{1-3\alpha}$. The fossil electrons have an index of $s \sim 1 - 1.5$ based on the PWN radio observation, thus, they should have a Lorentz factor $\gamma > \gamma_m$. Notice that the approximation of $t \gg t_0$ is used. Therefore, the fraction of electron with $> \gamma$ is

$$\zeta_e \simeq \frac{(\gamma/\gamma_m)^{1-s}}{1 + \alpha(s-1)} \sim \text{const. for } t \gg t_0. \quad (34)$$

For the range of α considered here, and considering that the electron population is dominated by the low-energy band, Eq. (2) yields

$$\gamma_c \propto \begin{cases} \gamma_m \left(\frac{t}{t_0} \right)^{1/2-\alpha} \propto R^{1/2\alpha-1}, & \text{for } \alpha > 1/2, \\ \gamma_m \sim \text{const.}, & \text{for } \alpha < 1/2. \end{cases} \quad (35)$$

For the free-expansion phase and Sedov-Taylor phase with a constant wind, one always has $\alpha > 1/2$, see Table 1 in detail. According to the predicted $L_\nu - |\text{RM}|$ relation, one finally has

$$L \propto \zeta_e \gamma_c^2 R^2 |\text{RM}| \propto R^\epsilon |\text{RM}| \quad \text{with } \epsilon = 1/\alpha. \quad (36)$$

This implies that $\alpha|\epsilon| = 1$, approximately consistent with the measured $\alpha|\epsilon| = 1.5 \pm 0.7$.

On the other hand, the spindown scenario with a decaying wind, $\dot{N}_e = \dot{N}_{e,0}(t/\tau)^{-2}$, where τ is the spindown timescale, typically arises at the late stages of supernova evolution, e.g., in the Sedov-Taylor phase. We assume $\alpha(s-1) < 1$ for the range of parameters considered here, and $t \gg \tau$ and $t \gg t_0$, then one has

$$\begin{aligned} N_e(\gamma, t) &= \frac{(s-1) \dot{N}_{e,0} \tau}{1 - \alpha(s-1) \gamma_m} \left(\frac{\tau}{t_0} \right)^{1-\alpha(s-1)} \left(\frac{t}{\tau} \right)^{-\alpha(s-1)} \\ &\times \left(\frac{\gamma}{\gamma_m} \right)^{-s} \quad \text{for } \gamma > \gamma_m(t/t_0)^{-\alpha}. \end{aligned} \quad (37)$$

Note that the rapid decay of the injection rate ensures that adiabatic cooling only shifts the injected power-law spectrum in energy without altering its slope, resulting in a single power-law fossil electron spectrum. Besides, when taking into account an injection rate that decays with time as t^{-2} , the denominator $1 - \alpha(s - 1)$ in the above formula differs from that $1 + \alpha(s - 1)$ in the case of steady injection. The fraction of electrons with Lorentz factor $> \gamma$ is

$$\zeta_e = \left(\frac{\gamma}{\gamma_m}\right)^{1-s} \left(\frac{t}{t_0}\right)^{-\alpha(s-1)} \propto R^{-(s-1)}. \quad (38)$$

Within the range of s of interest, one has

$$\gamma_c \propto \gamma_m \left(\frac{t}{t_0}\right)^{-\alpha} \propto R^{-1}. \quad (39)$$

For the Sedov-Taylor phase with a decaying wind, the temporal index of the nebula radius evolution is $\alpha = 3/10$, see Table 1 in detail. According to the predicted $L_\nu - |\text{RM}|$ relation, one finally has

$$L \propto \zeta_e \gamma_c^2 R^2 |\text{RM}| \propto R^\epsilon |\text{RM}| \quad \text{with } \epsilon \sim -(s - 1). \quad (40)$$

One finally has $\epsilon = 0, -0.5$ and $\alpha|\epsilon| = 0, 0.15$ for the fossil electron with $s = 1, 1.5$, respectively. All the above results are summarized in Table 4. In conclusion, the measured value of $\alpha|\epsilon| = 1.5 \pm 0.7$ disfavors old PWNe powered by a decaying wind and is instead more consistent with young PWNe driven by a nearly constant wind.

Table 4. The theoretical values of the combined index $\alpha|\epsilon|$ for various PWN bubble scenarios compared with the measured value of $\alpha|\epsilon| = 1.5 \pm 0.7$

		$\alpha \epsilon $	
		$s = 1.0$	$s = 1.5$
Constant Wind	Free-Expansion	1.0	1.0
Constant Wind	Sedov-Taylor	1.0	1.0
Decaying Wind	Sedov-Taylor	0.0	0.15

Although fossil electrons in a PWN bubble can naturally produce synchrotron radiation, a key issue concerns how the PWN contributes to the observable RM, since a relativistic pair plasma with a small amount of Goldreich-Julian net charge cannot generate a significant RM (Y.-P. Yang et al. 2023). However, theoretical modeling of PWN dynamics and X-ray morphology suggests that baryons are expected to be present in PWNe, as their inclusion is physically required to address the so-called “ σ

problem”: a wind composed purely of electron-positron pairs cannot efficiently convert the pulsar’s magnetic energy into the kinetic energy inferred at TS (C. F. Kennel & F. V. Coroniti 1984). Consequently, while electron-positron pairs dominate the particle number and the observable radiation, baryons are believed to carry a substantial fraction of the wind’s energy and to govern the large-scale dynamics of the nebula (M. Hoshino et al. 1992), potentially augmented by external material mixed in from the SN ejecta (J. M. Blondin et al. 2001). In this picture, the RM is expected to be contributed predominantly by the extra charge-neutralizing electrons associated with the baryonic component. Finally, because the PWN of a typical radio pulsar contributes a small value of RM, for a PRS to exhibit a significant RM in that region, the PWN would need to be atypical—for instance, a young PWN or a nebula dominated by magnetar winds (B. D. Metzger et al. 2019).

4.3. Bow shock in binary system

In a binary system, the accelerated relativistic electrons generate non-thermal radiation at: 1) companion-wind shock; 2) pulsar-wind shock, as shown in the panel (b) of Figure 2. First, for the pulsar-wind shock, different from that the fossil electrons in a PWN/SNR system survive for millions of years and are confined by the surrounding ejecta, the bow shock in a binary system, by contrast, are open and compact systems: particles are rapidly advected out of the shock region on a much shorter timescales, preventing any long-term accumulation. In this case, only a small fraction of the pulsar wind power is intercepted by the shock, and only a minor portion of that energy is transferred to electrons radiating at radio frequencies. On the other hand, for the companion-wind shock, since the shock velocity is only a few $\times 100 \text{ km s}^{-1}$, much less than that of the SNR shock, its synchrotron radiation would be much weaker. Due to the above reason, the radio luminosity of bow shocks is intrinsically low (e.g., $L \sim (10^{27} - 10^{30}) \text{ erg s}^{-1}$ with typical frequency of GHz, G. Dubus (2013); A. T. Deller et al. (2015)), although the magnetic field near the bow shock can be strong, making individual electrons radiate efficiently. As a result, the radio emission is governed by the instantaneous energy dissipation rather than by historical buildup, leading to radio luminosities several orders of magnitude lower than those of pulsar wind nebulae in supernova remnants. If the PRSs are produced by the bow shock in a binary system, the binary should be much closer and the companion should have a stronger wind. In any case, we briefly discuss this situation below.

Different from the nebula scenario discussed in Section 4.1, for the bow shock scenario in binary systems, the nebula radius mainly depends on the orbital separation and the pressure balance between the pulsar wind and the companion wind, rather than the nebula radius evolution. Thus, the scatter of the $L_\nu - |\text{RM}|$ relation is determined by the binary parameter. We assume that the orbital separations satisfy a power-law distribution

$$f(a) \propto a^{-\kappa_a}, \quad (41)$$

where $\kappa_a = 1$ corresponds to the Öpik with $f(\log a) = \text{const.}$ Based on pressure balance, the bow shock is located at a distance R from the neutron star,

$$R = \frac{\sqrt{\eta_w}}{1 + \sqrt{\eta_w}} a \quad \text{with } \eta_w \equiv \frac{L_{\text{sd}}}{\dot{M}_w v_w c}, \quad (42)$$

where L_{sd} is the spindown luminosity of the neutron star, \dot{M}_w is the mass loss rate of the companion, v_w is the velocity of the companion wind. We assume that η_w is independent of the orbital separation a , then the shock radius satisfies the distribution of

$$f(R) \propto R^{-\kappa_a}. \quad (43)$$

On the other hand, the energy distribution of the accelerated electrons in both the shocked pair wind side and the shocked companion wind side mainly depends on the properties of the bow shock with parameter $L_{\text{sd}}, \dot{M}_w, v_w$. Both ζ_e and γ_c are expected to be largely independent of R , as the bow-shock system is open, allowing cooling electrons to escape. Consider that the $L_\nu - |\text{RM}|$ relation is more sensitive to R , the scatter of the relation might mainly determined by $f(R) \propto R^{-\kappa_a}$. According to the predicted $L_\nu - |\text{RM}|$ relation, one finally has

$$L \propto \zeta_e \gamma_c^2 R^2 |\text{RM}| \propto R^\epsilon |\text{RM}| \quad \text{with } \epsilon = 2. \quad (44)$$

By combining with Eq.(9), we define $\tilde{\alpha} \equiv 1/(1 - \kappa_a)$ and one finally has $\tilde{\alpha}|\epsilon| = 2/(1 - \kappa_a)$. Notice that although the bow shock radius does not evolve with time, its statistical distribution among the population mathematically mimics the temporal evolution of an expanding nebula. Therefore, we can equate its spatial distribution index $\tilde{\alpha}$ to the effective temporal index α to utilize the same statistical framework. By equating this spatial distribution index $\tilde{\alpha}$ to the effective variance parameter α derived from our scatter framework, one finally has $\kappa_a = -0.34 \pm 0.60$.

The derived value has large uncertainties and is marginally consistent with a flat distribution ($\kappa_a \sim 0$) or even Öpik's law ($\kappa_a \sim 1$) within 2σ . Therefore, the binary wind scenario cannot be ruled out solely based on this statistical argument. However, a more critical issue

is the selection bias: radio luminosity is expected to drop significantly with separation a , meaning a flux-limited sample should be dominated by close binaries. Furthermore, we note that our derivation assumes a steady formation rate and an unbiased sampling of the PRS population. In reality, flux-limited surveys may suffer from Malmquist bias, preventing the detection of older, fainter, and larger nebulae.

5. CONCLUSION

Building upon the unified framework established by Y.-P. Yang et al. (2020, 2022), we introduce in this work a novel statistical approach to diagnose the physical properties of these environments. Here, we demonstrate that the intrinsic scatter of this relation is not merely measurement noise but a valuable physical probe encoding the dynamical evolution of the nebula radius ($R \propto t^\alpha$). As future surveys increase the sample size, this method will enable direct constraints on the age distribution and evolutionary history of FRB environments. Ultimately, this approach provides a new pathway to probing the life cycle of magnetars and their surrounding nebulae. By deriving a generic scaling of $L_\nu \propto R^\epsilon |\text{RM}|$ and analyzing the residuals of the five currently confirmed FRB-PRS systems relative to the theoretical baseline, we successfully constrained the combined evolutionary index to be $\alpha|\epsilon| = 1.5 \pm 0.7$.

This new diagnostic method allows us to effectively discriminate between different astrophysical scenarios based on the population statistics. In particular, the inferred value deviates from the ranges predicted for several systems. For example, SNRs in the Sedov–Taylor phase typically yield $\alpha|\epsilon| \sim 0.2\text{--}0.4$, and reverse shocks in SNR/ISM systems during the free-expansion stage are predicted to produce large values of $\alpha|\epsilon| \gtrsim 3.5$. Furthermore, PWNe powered by a decaying pulsar wind generally correspond to very small values of $\alpha|\epsilon| \sim 0\text{--}0.15$. The measured value of $\alpha|\epsilon| = 1.5 \pm 0.7$ therefore falls outside the characteristic ranges associated with these scenarios. Instead, it lies broadly within or closer to the ranges expected for forward shocks propagating during the free-expansion phase, either in SNR/ISM systems or in PWN/SNR systems, where theoretical estimates give $\alpha|\epsilon| \sim 2.0\text{--}2.8$. It is also consistent with the expectations for young PWNe driven by an approximately constant pulsar wind, which typically predict $\alpha|\epsilon| \sim 1$. These initial constraints tentatively favor the physical picture where active repeaters are powered by dynamically young, rapidly expanding nebulae (likely less than centuries old). While a binary bow-shock origin remains a mathematically plausible alternative depending on the orbital distribution, its inherently low radio luminosity

implies that flux-limited samples would be heavily biased toward extremely close binaries, which contradicts the broad dispersion observed in the sample. Therefore, the current result more naturally supports the scenario of young, expanding SNRs or PWN bubbles.

We acknowledge that the current sample size ($N = 5$) limits the statistical significance of these constraints, and future observations are needed to refine the evolutionary index. However, the scatter-analysis framework established here serves as a powerful, independent tool to map the evolutionary timeline of FRB sources. As next-generation radio surveys localize a larger population of repeating FRBs, this method will enable us to distinguish between various progenitor channels and

trace the life cycle of the central engines by simply analyzing the dispersion in their $L_\nu - |\text{RM}|$ phase space.

ACKNOWLEDGES

This independent work marks the 10th anniversary of the author's collaboration with Bing Zhang, originating from their early study on synchrotron-heated nebulae – a theoretical exploration that predated the discovery of the first FRB-associated PRS. The author also acknowledges the helpful discussions with Yue Wu, Chen-Hui Niu, Gabriele Bruni and Rui-Nan Li. This work is supported by the National Natural Science Foundation of China (No. 12473047), the National Key Research and Development Program of China (No. 2024YFA1611603) and the Yunnan Key Laboratory of Survey Science (No. 202449CE340002).

REFERENCES

- An, T., Wang, A., Huang, Y.-C., et al. 2025, *ApJL*, 991, L20, doi: [10.3847/2041-8213/ae0324](https://doi.org/10.3847/2041-8213/ae0324)
- Anna-Thomas, R., Connor, L., Dai, S., et al. 2023, *Science*, 380, 599, doi: [10.1126/science.abo6526](https://doi.org/10.1126/science.abo6526)
- Atoyan, A. M., & Aharonian, F. A. 1996, *MNRAS*, 278, 525, doi: [10.1093/mnras/278.2.525](https://doi.org/10.1093/mnras/278.2.525)
- Bhardwaj, M., Gaensler, B. M., Kaspi, V. M., et al. 2021, *ApJL*, 910, L18, doi: [10.3847/2041-8213/abeaa6](https://doi.org/10.3847/2041-8213/abeaa6)
- Bhusare, Y., Maan, Y., & Kumar, A. 2025, *ApJ*, 993, 234, doi: [10.3847/1538-4357/ae0451](https://doi.org/10.3847/1538-4357/ae0451)
- Blondin, J. M., Chevalier, R. A., & Frierson, D. M. 2001, *ApJ*, 563, 806, doi: [10.1086/324042](https://doi.org/10.1086/324042)
- Bochenek, C. D., Ravi, V., Belov, K. V., et al. 2020, *Nature*, 587, 59, doi: [10.1038/s41586-020-2872-x](https://doi.org/10.1038/s41586-020-2872-x)
- Bruni, G., Piro, L., Yang, Y.-P., et al. 2024, *Nature*, 632, 1014, doi: [10.1038/s41586-024-07782-6](https://doi.org/10.1038/s41586-024-07782-6)
- Bruni, G., Piro, L., Yang, Y.-P., et al. 2025, *A&A*, 695, L12, doi: [10.1051/0004-6361/202453233](https://doi.org/10.1051/0004-6361/202453233)
- Chatterjee, S., Law, C. J., Wharton, R. S., et al. 2017, *Nature*, 541, 58, doi: [10.1038/nature20797](https://doi.org/10.1038/nature20797)
- CHIME/FRB Collaboration, Andersen, B. C., Bandura, K. M., et al. 2020, *Nature*, 587, 54, doi: [10.1038/s41586-020-2863-y](https://doi.org/10.1038/s41586-020-2863-y)
- CHIME/FRB Collaboration, Amiri, M., Andersen, B. C., et al. 2021, *ApJS*, 257, 59, doi: [10.3847/1538-4365/ac33ab](https://doi.org/10.3847/1538-4365/ac33ab)
- Dai, Z. G., Wang, J. S., & Yu, Y. W. 2017, *ApJL*, 838, L7, doi: [10.3847/2041-8213/aa6745](https://doi.org/10.3847/2041-8213/aa6745)
- Deller, A. T., Moldon, J., Miller-Jones, J. C. A., et al. 2015, *ApJ*, 809, 13, doi: [10.1088/0004-637X/809/1/13](https://doi.org/10.1088/0004-637X/809/1/13)
- Dong, Y., Eftekhari, T., Fong, W., et al. 2024, *ApJ*, 973, 133, doi: [10.3847/1538-4357/ad6568](https://doi.org/10.3847/1538-4357/ad6568)
- Dubus, G. 2013, *A&A Rv*, 21, 64, doi: [10.1007/s00159-013-0064-5](https://doi.org/10.1007/s00159-013-0064-5)
- Eftekhari, T., Berger, E., Margalit, B., Metzger, B. D., & Williams, P. K. G. 2020, *ApJ*, 895, 98, doi: [10.3847/1538-4357/ab9015](https://doi.org/10.3847/1538-4357/ab9015)
- Fong, W.-f., Dong, Y., Leja, J., et al. 2021, *ApJL*, 919, L23, doi: [10.3847/2041-8213/ac242b](https://doi.org/10.3847/2041-8213/ac242b)
- Frail, D. A., & Scharringhausen, B. R. 1997, *ApJ*, 480, 364, doi: [10.1086/303943](https://doi.org/10.1086/303943)
- FRB Collaboration, Abbott, T., Andersen, B. C., et al. 2026, arXiv e-prints, arXiv:2601.09399, doi: [10.48550/arXiv.2601.09399](https://doi.org/10.48550/arXiv.2601.09399)
- Gaensler, B. M., & Slane, P. O. 2006, *ARA&A*, 44, 17, doi: [10.1146/annurev.astro.44.051905.092528](https://doi.org/10.1146/annurev.astro.44.051905.092528)
- Gao, R., Gao, H., Li, Z., & Yang, Y.-P. 2025, *ApJ*, 994, 239, doi: [10.3847/1538-4357/ae1a7d](https://doi.org/10.3847/1538-4357/ae1a7d)
- Hilmarsson, G. H., Michilli, D., Spitler, L. G., et al. 2021, *ApJL*, 908, L10, doi: [10.3847/2041-8213/abdec0](https://doi.org/10.3847/2041-8213/abdec0)
- Hoshino, M., Arons, J., Gallant, Y. A., & Langdon, A. B. 1992, *ApJ*, 390, 454, doi: [10.1086/171296](https://doi.org/10.1086/171296)
- Ibik, A. L., Drout, M. R., Gaensler, B. M., et al. 2024, *ApJ*, 961, 99, doi: [10.3847/1538-4357/ad0893](https://doi.org/10.3847/1538-4357/ad0893)
- Kennel, C. F., & Coroniti, F. V. 1984, *ApJ*, 283, 694, doi: [10.1086/162356](https://doi.org/10.1086/162356)
- Kirsten, F., Marcote, B., Nimmo, K., et al. 2022, *Nature*, 602, 585, doi: [10.1038/s41586-021-04354-w](https://doi.org/10.1038/s41586-021-04354-w)
- Kremer, K., Piro, A. L., & Li, D. 2021, *ApJL*, 917, L11, doi: [10.3847/2041-8213/ac13a0](https://doi.org/10.3847/2041-8213/ac13a0)
- Li, C. K., Lin, L., Xiong, S. L., et al. 2021, *Nature Astronomy*, 5, 378, doi: [10.1038/s41550-021-01302-6](https://doi.org/10.1038/s41550-021-01302-6)
- Li, Q.-C., Yang, Y.-P., & Dai, Z.-G. 2020, *ApJ*, 896, 71, doi: [10.3847/1538-4357/ab8db8](https://doi.org/10.3847/1538-4357/ab8db8)

- Lu, W., Beniamini, P., & Kumar, P. 2022, *MNRAS*, 510, 1867, doi: [10.1093/mnras/stab3500](https://doi.org/10.1093/mnras/stab3500)
- Marcote, B., Paragi, Z., Hessels, J. W. T., et al. 2017, *ApJL*, 834, L8, doi: [10.3847/2041-8213/834/2/L8](https://doi.org/10.3847/2041-8213/834/2/L8)
- Margalit, B., & Metzger, B. D. 2018, *ApJL*, 868, L4, doi: [10.3847/2041-8213/aaedad](https://doi.org/10.3847/2041-8213/aaedad)
- McKee, C. F., & Truelove, J. K. 1995, *PhR*, 256, 157, doi: [10.1016/0370-1573\(94\)00106-D](https://doi.org/10.1016/0370-1573(94)00106-D)
- Mereghetti, S., Savchenko, V., Ferrigno, C., et al. 2020, *ApJL*, 898, L29, doi: [10.3847/2041-8213/aba2cf](https://doi.org/10.3847/2041-8213/aba2cf)
- Metzger, B. D., Berger, E., & Margalit, B. 2017, *ApJ*, 841, 14, doi: [10.3847/1538-4357/aa633d](https://doi.org/10.3847/1538-4357/aa633d)
- Metzger, B. D., Margalit, B., & Sironi, L. 2019, *MNRAS*, 485, 4091, doi: [10.1093/mnras/stz700](https://doi.org/10.1093/mnras/stz700)
- Michilli, D., Seymour, A., Hessels, J. W. T., et al. 2018, *Nature*, 553, 182, doi: [10.1038/nature25149](https://doi.org/10.1038/nature25149)
- Moroianu, A. M., Bhandari, S., Drout, M. R., et al. 2026, *ApJL*, 996, L16, doi: [10.3847/2041-8213/ae28c7](https://doi.org/10.3847/2041-8213/ae28c7)
- Murase, K., Kashiyama, K., & Mészáros, P. 2016, *MNRAS*, 461, 1498, doi: [10.1093/mnras/stw1328](https://doi.org/10.1093/mnras/stw1328)
- Niu, C.-H., Aggarwal, K., Li, D., et al. 2022, *Nature*, 606, 873, doi: [10.1038/s41586-022-04755-5](https://doi.org/10.1038/s41586-022-04755-5)
- Niu, C.-H., Li, D., Yang, Y.-P., et al. 2026, *Science Bulletin*, 71, 76, doi: [10.1016/j.scib.2025.11.023](https://doi.org/10.1016/j.scib.2025.11.023)
- Planck Collaboration, Aghanim, N., Akrami, Y., et al. 2020, *A&A*, 641, A6, doi: [10.1051/0004-6361/201833910](https://doi.org/10.1051/0004-6361/201833910)
- Quataert, E., & Gruzinov, A. 2000, *ApJ*, 545, 842, doi: [10.1086/317845](https://doi.org/10.1086/317845)
- Rahaman, S. M., Acharya, S. K., Beniamini, P., & Granot, J. 2025, *ApJ*, 988, 276, doi: [10.3847/1538-4357/ade70c](https://doi.org/10.3847/1538-4357/ade70c)
- Reines, A. E., Condon, J. J., Darling, J., & Greene, J. E. 2020, *ApJ*, 888, 36, doi: [10.3847/1538-4357/ab4999](https://doi.org/10.3847/1538-4357/ab4999)
- Reynolds, S. P., & Chevalier, R. A. 1984, *ApJ*, 278, 630, doi: [10.1086/161831](https://doi.org/10.1086/161831)
- Ridnaia, A., Svinkin, D., Frederiks, D., et al. 2021, *Nature Astronomy*, 5, 372, doi: [10.1038/s41550-020-01265-0](https://doi.org/10.1038/s41550-020-01265-0)
- Sridhar, N., & Metzger, B. D. 2022, *ApJ*, 937, 5, doi: [10.3847/1538-4357/ac8a4a](https://doi.org/10.3847/1538-4357/ac8a4a)
- Tavani, M., Casentini, C., Ursi, A., et al. 2021, *Nature Astronomy*, 5, 401, doi: [10.1038/s41550-020-01276-x](https://doi.org/10.1038/s41550-020-01276-x)
- Tendulkar, S. P., Bassa, C. G., Cordes, J. M., et al. 2017, *ApJL*, 834, L7, doi: [10.3847/2041-8213/834/2/L7](https://doi.org/10.3847/2041-8213/834/2/L7)
- Tian, J., Rajwade, K. M., Pastor-Marazuela, I., et al. 2024, *MNRAS*, 533, 3174, doi: [10.1093/mnras/stae2013](https://doi.org/10.1093/mnras/stae2013)
- van der Swaluw, E., Achterberg, A., Gallant, Y. A., & Tóth, G. 2001, *A&A*, 380, 309, doi: [10.1051/0004-6361:20011437](https://doi.org/10.1051/0004-6361:20011437)
- Wang, F. Y., Zhang, G. Q., Dai, Z. G., & Cheng, K. S. 2022, *Nature Communications*, 13, 4382, doi: [10.1038/s41467-022-31923-y](https://doi.org/10.1038/s41467-022-31923-y)
- Wang, J.-S., Yang, Y.-P., Wu, X.-F., Dai, Z.-G., & Wang, F.-Y. 2016, *ApJL*, 822, L7, doi: [10.3847/2041-8205/822/1/L7](https://doi.org/10.3847/2041-8205/822/1/L7)
- Wang, P., Zhang, J. S., Yang, Y. P., et al. 2025, *arXiv e-prints*, arXiv:2507.15790, doi: [10.48550/arXiv.2507.15790](https://doi.org/10.48550/arXiv.2507.15790)
- Xu, H., Niu, J. R., Chen, P., et al. 2022, *Nature*, 609, 685, doi: [10.1038/s41586-022-05071-8](https://doi.org/10.1038/s41586-022-05071-8)
- Yang, A. Y., Feng, Y., Tsai, C.-W., et al. 2024, *ApJ*, 976, 165, doi: [10.3847/1538-4357/ad7d02](https://doi.org/10.3847/1538-4357/ad7d02)
- Yang, Y.-H., & Dai, Z.-G. 2019, *ApJ*, 885, 149, doi: [10.3847/1538-4357/ab48dd](https://doi.org/10.3847/1538-4357/ab48dd)
- Yang, Y.-P., Li, Q.-C., & Zhang, B. 2020, *ApJ*, 895, 7, doi: [10.3847/1538-4357/ab88ab](https://doi.org/10.3847/1538-4357/ab88ab)
- Yang, Y.-P., Lu, W., Feng, Y., Zhang, B., & Li, D. 2022, *ApJL*, 928, L16, doi: [10.3847/2041-8213/ac5f46](https://doi.org/10.3847/2041-8213/ac5f46)
- Yang, Y.-P., Xu, S., & Zhang, B. 2023, *MNRAS*, 520, 2039, doi: [10.1093/mnras/stad168](https://doi.org/10.1093/mnras/stad168)
- Yang, Y.-P., Zhang, B., & Dai, Z.-G. 2016, *ApJL*, 819, L12, doi: [10.3847/2041-8205/819/1/L12](https://doi.org/10.3847/2041-8205/819/1/L12)
- Zhang, B. 2020, *ApJL*, 890, L24, doi: [10.3847/2041-8213/ab7244](https://doi.org/10.3847/2041-8213/ab7244)
- Zhang, B. 2023, *Reviews of Modern Physics*, 95, 035005, doi: [10.1103/RevModPhys.95.035005](https://doi.org/10.1103/RevModPhys.95.035005)
- Zhang, B. 2024, *Annual Review of Nuclear and Particle Science*, 74, 89, doi: [10.1146/annurev-nucl-102020-124444](https://doi.org/10.1146/annurev-nucl-102020-124444)
- Zhang, B., & Hu, R.-C. 2025, *ApJL*, 994, L20, doi: [10.3847/2041-8213/ae1023](https://doi.org/10.3847/2041-8213/ae1023)
- Zhang, J.-S., Wang, T.-C., Wang, P., et al. 2025, *arXiv e-prints*, arXiv:2507.14707, doi: [10.48550/arXiv.2507.14707](https://doi.org/10.48550/arXiv.2507.14707)
- Zhang, L., Chen, S. B., & Fang, J. 2008, *ApJ*, 676, 1210, doi: [10.1086/527466](https://doi.org/10.1086/527466)
- Zhang, X., Yu, W., Yan, Z., Xing, Y., & Zhang, B. 2025, *arXiv e-prints*, arXiv:2501.14247, doi: [10.48550/arXiv.2501.14247](https://doi.org/10.48550/arXiv.2501.14247)
- Zhang, Z.-L., & Zhang, B. 2025, *ApJL*, 984, L40, doi: [10.3847/2041-8213/adcc30](https://doi.org/10.3847/2041-8213/adcc30)